Laboratory demonstration of static-mode down-looking synthetic aperture imaging ladar

Zhiyong Lu (卢智勇), Ning Zhang (张 宁), Jianfeng Sun (孙建锋)*, Yu Zhou (周 煜), Zhu Luan (栾 竹), Guangyu Cai (蔡光宇), and Liren Liu (刘立人)

Key Laboratory of Space Laser Communication and Detection Technology, Shanghai Institute of Optics and Fine Mechanics, Chinese Academy of Sciences, Shanghai, 201800, China

**Corresponding author: sunjianfengs@163.com*

Received November 16, 2014; accepted January 28, 2015; posted online March 10, 2015

A static-mode synthetic aperture imaging ladar (SAIL) in which the target and carrying platform are kept still during the collection process is proposed and demonstrated. A target point of 0.5 mm × 0.5 mm and a two-dimensional (2D) object are reconstructed in the experiments, in which an optical collimator with a focal length of 10 m is used to simulate the far-field condition. The achieved imaging resolution is in agreement with the theoretical design. The static-mode down-looking SAIL has the capability to eliminate the influence from the atmospheric turbulence and can be conveniently operated outdoors.

OCIS codes: 280.6730, 280.3640, 100.2000, 100.3010, 110.0110.
doi: 10.3788/COL201513.042801.

A synthetic aperture imaging ladar (SAIL) can provide fine resolution, two-dimensional (2D) active imaging at a long range with small-diameter optics. It recently became an interesting field of research, and two kinds of SAILs, the side-looking SAIL and the down-looking SAIL, have been reported[1–10]. The side-looking SAIL has the disadvantages of a narrow footprint, serious phase interferences from atmospheric turbulence, and mechanical trembling. Meanwhile, in order to control the phase, some very complicated technology must be used in the side-looking SAIL, such as a matched optical delay line to guarantee the beat frequencies from heterodyne to a reasonable range or a hydrogen cyanide cell to synchronize the initial phase[1,2]. However, the down-looking SAIL significantly relaxes the difficulties faced when using the side-looking SAIL.

The down-looking SAIL is based on the key ideas of wavefront transformation and regulation by optical techniques, with a transmitter of two coaxial and orthogonal-polarization beams, and a receiver of self-heterodyne detection. In the orthogonal direction of travel, a linear phase modulation proportional to the lateral distance of the target point is generated by scanning two cylindrical lenses with the same curvatures of the wavefront in reverse. A quadratic phase history centered in the longitudinal position of the target point in the travel direction is produced by using another two cylindrical lenses with different curvatures of the wavefront. The image is focused by the Fourier transform and matched filtering in the two respective directions. The down-looking SAIL has as its inherent feature a controllable and changeable size of the optical footprint, which, together with the associated imaging resolution, can be, manipulated on a large scale. Meanwhile, it effectively reduces the influence of atmospheric turbulence, and simplifies the system structure. Clearly, the down-looking SAIL would be appropriate for practical uses.

In this Letter, we propose the concept of a static-mode down-looking SAIL based on the previous down-looking SAIL[11,12]. We keep the target and carrying platform still. Two cylindrical lenses with the same curvatures of the wavefront are scanned to produce a linear phase modulation. Another cylindrical lens is moved slowly along the direction of travel to produce a quadratic phase history, instead of moving the carrying platform. In the laboratory, a point image and a 2D image are reconstructed under simulated far-field conditions with an optical collimator that has a focal length of 10 m. In particular, the static mode is unique in the down-looking SAIL; it is difficult to implement in the traditional microwave synthetic aperture radar (SAR) and the side-looking SAIL.

The schematic diagram of the static-mode SAIL system is illustrated in Fig. 1. It consists of a transmitter, an optical collimator, a receiver, and a personal computer (PC). The transmitter is composed of a laser source, a half-wave plate, lens L1, cylinder lenses L2, L3, and L4, two polarization beam splitters (PBSs, one acting as a splitter, the other as a combiner), two quarter- wave plates, four mirrors, two drive motors, signal generators, and the main lens. Lens L1 is used to adjust the size of the inner beam. Cylinder lenses L2, L3, and L4 are placed on the focal plane of the main lens. L2 and L3 are the x-direction cylinder lenses, and L4 is the y-direction cylinder lens that is close to L2. The shift of L2 and L3 produces a linear phase in the orthogonal direction of travel. L2 and L3 have a bias of pre-arranged shift S_b in order to move the position of the reconstructed image. L4 is used to generate a spatial quadratic phase history in the travel direction. The receiver is composed of a receiving telescope, a half-wave plate, one PBS, two mini-lenses, a balanced receiver, and a digitizer. The signal generators in the transmitter and the digitizer in the receiver are connected and controlled correctly by the PC.

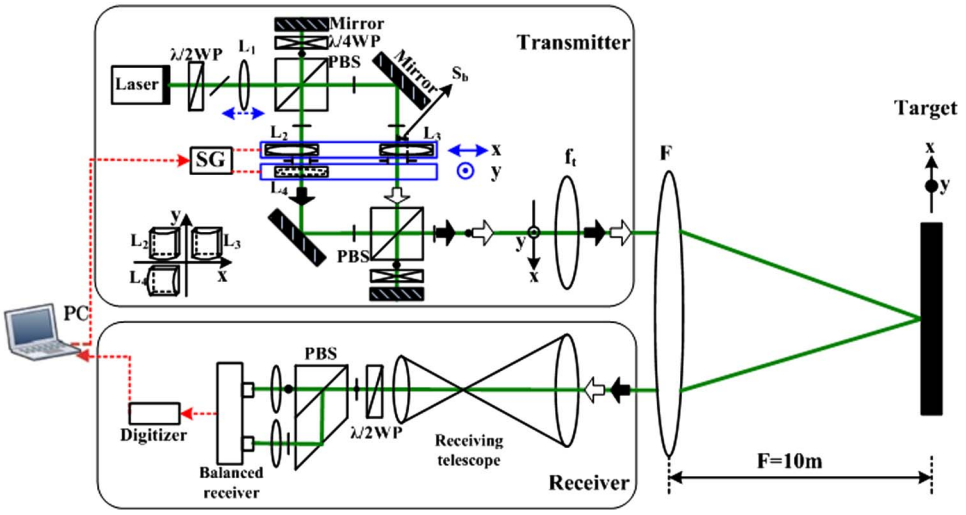

Fig. 1. Experimental structure for static-mode down-looking SAIL imaging.

In our experiment, cylinder lens L2 and cylinder lens L3 scan periodically with a fast velocity. Meanwhile, cylinder lens L4 moves along the y-direction with a slow velocity. Based on this information, we have the inner optical fields at the focal plane of the main lens as

$$
\begin{aligned}
&e_R(x, y{:}t_{f,n}, t_{s,m}) \\
&= E_0 \operatorname{rect}\left(\frac{t_{f,n}}{T_f}\right)\operatorname{rect}\left(\frac{t_{s,m}}{T_s}\right)\operatorname{rect}\left(\frac{x}{W_x}\right)\operatorname{rect}\left(\frac{y}{W_y}\right) \\
&\quad \times \exp\left[-j\frac{\pi}{\lambda f_x}(x - v_x t_{f,n} - S_b)^2\right] \\
&\quad \times \exp\left[-j\frac{\pi}{\lambda f_y}(y - v_y t_{s,m})^2\right], \\
&e_L(x, y{:}t_{f,n}, t_{s,m}) \\
&= E_0 \operatorname{rect}\left(\frac{t_{f,n}}{T_f}\right)\operatorname{rect}\left(\frac{t_{s,m}}{T_s}\right)\operatorname{rect}\left(\frac{x}{W_x}\right)\operatorname{rect}\left(\frac{y}{W_y}\right) \\
&\quad \times \exp\left[-j\frac{\pi}{\lambda f_x}(x + v_x t_{f,n} - S_b)^2\right], \qquad (1)
\end{aligned}
$$

where $W_x \times W_y$ is the size of the inner beam, $t_{f,n}$ is the fast scanning time, v_x is the scanning velocity in the x-direction, and T_f is the scanning period, which begins at $-\frac{T_f}{2}$ and ends at $\frac{T_f}{2}$. $t_{s,m}$ is the slow-moving time, v_y is the moving velocity in y-direction, and the moving time is T_s, beginning from $-\frac{T_s}{2}$ and ending at $\frac{T_s}{2}$. S_b is the distance between the center of cylinder lens L2 (L3) and the corresponding propagation beam.

Via an amplified transmission, the inner field is imaged onto the focal plane of the optical collimator with an amplification factor of $M = F/f_t$. The reflected field from a target element at (x_p, y_p) was collected by the receiving telescope, optical hybrid, and the balanced receiver, sequentially. The optical power was simply the integration of the intensity over the receiving aperture. The resulting photocurrents from the 1×2 180° optical hybrid can be expressed by a radar equation for point targets, as follows:

$$
\begin{aligned}
&i_b(x_p, y_p{:}t_{f,n}, t_{s,m}) \\
&= E_r \operatorname{rect}\left(\frac{t_{f,n}}{T_f}\right)\operatorname{rect}\left(\frac{t_{s,m}}{T_s}\right)\operatorname{rect}\left(\frac{x_p}{MW_x}\right)\operatorname{rect}\left(\frac{y_p}{MW_y}\right) \\
&\quad \times \cos\left[-\frac{2\pi}{M^2\lambda f_x}(2(x_p + MS_b)Mv_x t_f)\right. \\
&\quad \left. - \frac{\pi}{M^2\lambda f_y/2}(y_p + Mv_y t_{s,m})^2\right], \qquad (2)
\end{aligned}
$$

where E_r includes all factors of transmission, propagation, and optical-to-electrical conversion.

During the imaging process, the 2D data was first compressed by the Fourier transform before the target frequency was extracted with a band-pass filter. Then, the 2D data was compressed by a match filter with a conjugate quadratic phase of the phase history in the travel direction.

A static-mode down-looking SAIL demonstration with an optical collimator that has a focal length of 10 m was designed, and the target and carrying platform are relatively static. A Gaussian beam with a wavelength of 532 nm and a power of 100 mW was used in the experiments. A positive lens with a focal length of 100 mm (L1) was used to adjust the orthogonal-polarization beams' size. The focal lengths of the three cylindrical lenses are all 60 mm, and the size of the lenses are all 14 mm × 14 mm. The scanning velocity of cylindrical lens L2 and cylindrical lens L3 was 2 mm/s, while lens L4 was actuated at 0.0025 mm/s. As a consequence, two coaxial and orthogonal-polarization beams with a spatial parabolic phase difference on the focal plane of the main lens were produced. As illustrated in Fig. 2, the parabolic phase difference is linear in the fast time direction and quadratic in the slow time direction. The main lens has a diameter of Φ155.5 mm and a focal length of 500 mm.

The diameter of the Gaussian illumination spot on the target plane was about 40 mm. The target was placed on the focal plane of the optical collimator, and the focal

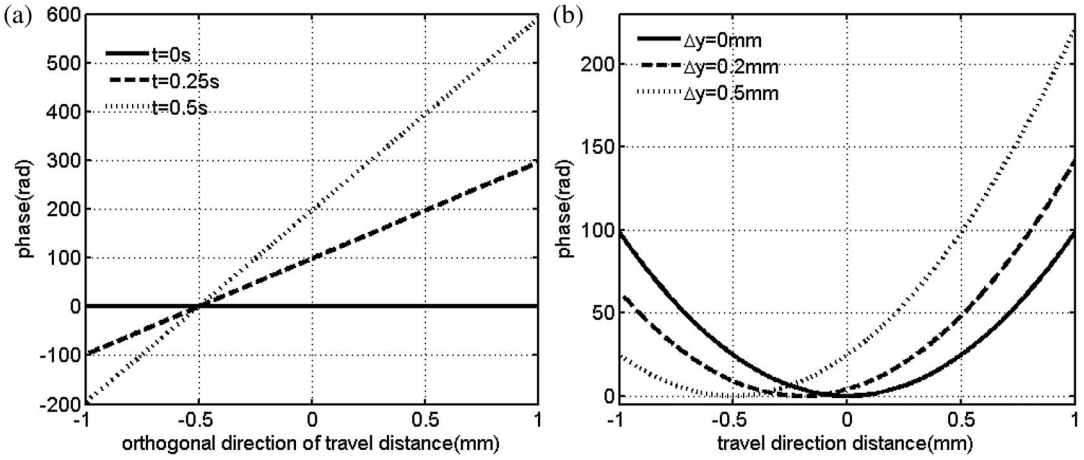

Fig. 2. The phase difference in the inner optical fields. (a) Orthogonal direction of travel. (b) Travel direction.

length was 10 m. The targets were made of 3M reflective sheets. The scattered light from the target was collected and collimated by a 155.5 mm diameter-receiving telescope. Two mini-lenses were placed after the 180° hybrid to focus the light towards the detectors of the balanced receivers.

The theoretical resolution in the orthogonal direction of travel is inversely proportional to the scanning range of the cylindrical lenses[8]. A scanning range of 1.2 mm was used in experiment, so the corresponding theoretical resolution is 0.53 mm. Similarly, the corresponding theoretical resolution in the travel direction is 0.73 mm under the moving range of 1.5 mm. A 0.5 mm × 0.5 mm target point was reconstructed in the experiments. Figure 3(a) shows the origin return signal, and Fig. 3(b) is the image that is focused by the Fourier transform in the orthogonal direction of travel. Figure 3(c) shows a quadratic phase history along the travel direction. Figure 3(d) is the reconstructed image, which is consistent with the dimension of the target. The resulting image has the full width at minimum of 0.8 mm × 1.1 mm, as shown in Figs. 3(e) and 3(f). The deviation from the theoretical calculation is mainly due to the nonlinearity of the lens shifting and the phase error of the inner optical fields. The phase error is caused by the cylindrical lens aberration and assembly position error.

The imaging experiments of 2D targets were operated under the same conditions, as shown in Fig. 4. The target was cut out from a retro reflective material as multi-strips

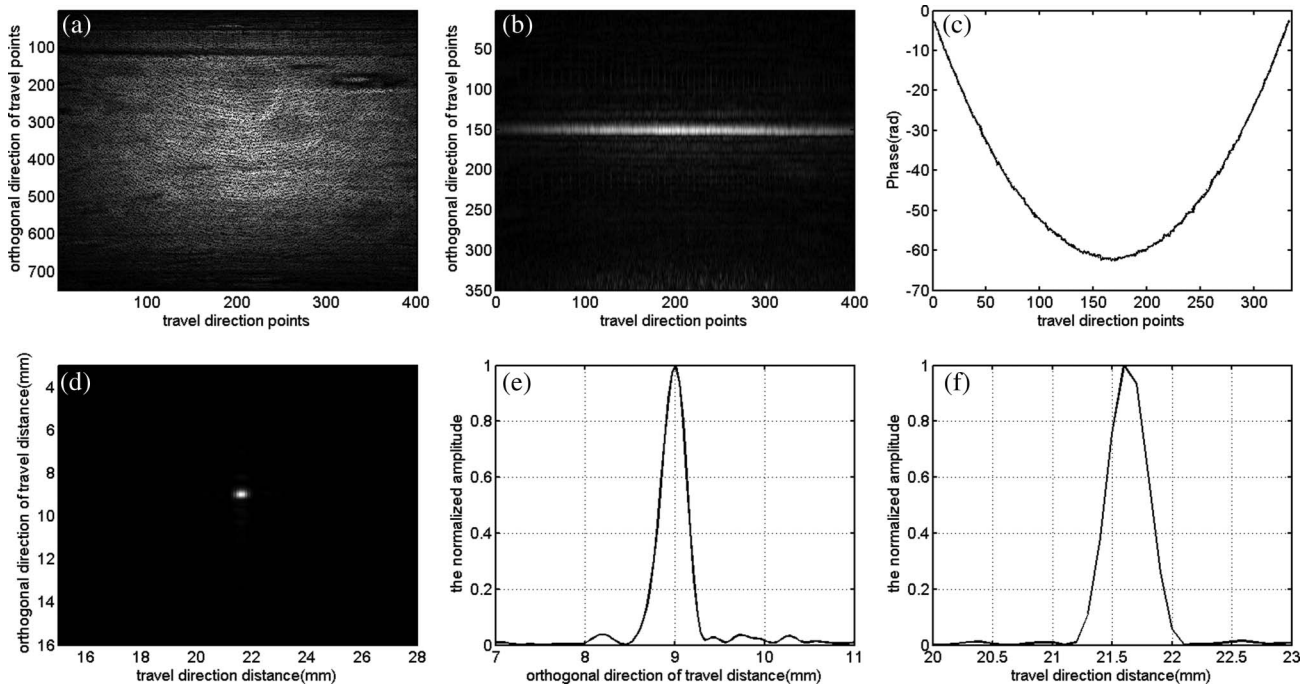

Fig. 3. Reconstructed image process of a point. (a) Return signal data. (b) The image focused by the Fourier transform. (c) Quadratic phase in the travel direction. (d) Reconstructed point image by matching filtering. (e) Point spread functions in the orthogonal direction of travel. (f) Point spread functions in the travel direction.

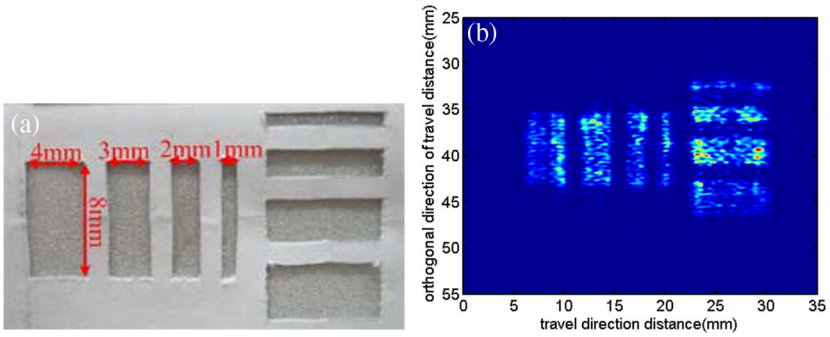

Fig. 4. Target image of multi-strips. (a) Actual image. (b) Reconstructed image.

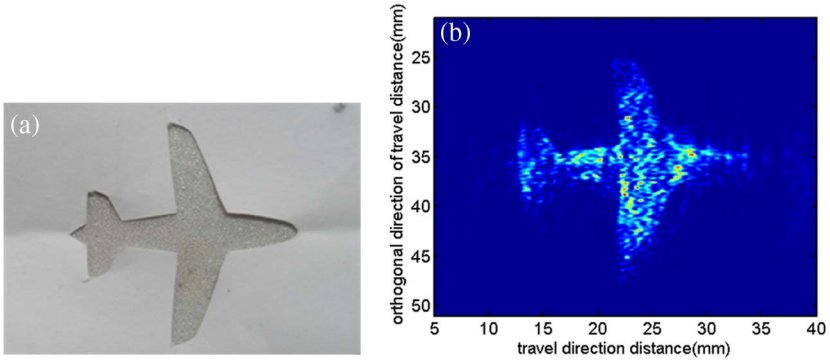

Fig. 5. Target image of planar plane. (a) Actual image. (b) Reconstructed image.

with lengths of 1, 2, 3, and 4 mm and a width of 8 mm, as shown in Fig. 4(a). The target was mounted on a plate at a 90° angle to the incidence beam. The reconstructed image is depicted in Fig. 4(b). Likewise, a reconstructed 23 mm × 20 mm planar plane is also displayed in Fig. 5. As predicted, the speckle effect is observed here. It is the residual effect caused by the randomly varied amplitudes of the returned optical field after random phases were canceled by the down-looking SAIL mechanism[13].

It should be emphasized that the static-mode down-looking SAIL uses an optical collimator to simulate the far-field situation due to the limitations of the laboratory site. The static-mode down-looking SAIL has the ability to automatically compensate for the influence of atmospheric turbulence and unmodeled line-of-sight motion, similar to the previous down-looking SAIL. As a consequence, the static-mode down-looking SAIL could be used outdoors.

In conclusion, we present a static-mode down-looking SAIL and its imaging experiments using an optical collimator with a 10 m focal length to simulate the far-field condition. The resolution is 0.8 mm × 1.1 mm, close to the theoretical design, and the 2D object is also reconstructed with a high contrast. Based on this work, we will develop a spotlight-mode down-looking SAIL, which will deploy a deflector to point to the target when the flight platform is moving along the travel direction. Under that mode, the resolution along the travel direction will be further improved, and the received power will also be enhanced.

This work was supported by the National Nature Science Foundation of China (Grant Nos. 61275110 and 61108069) and the Key Laboratory of Space Laser Communication and Detection Technology of the Chinese Academy of Sciences.

References

1. M. Bashkansky, R. L. Lucke, E. Funk, L. J. Rickard, and J. Reintjes, Opt. Lett. **27**, 1983 (2002).
2. S. M. Beck, J. R. Buck, W. F. Buell, R. P. Dickinson, D. A. Kozlowski, N. J. Marechal, and T. J. Wright, Appl. Opt. **44**, 7621 (2005).
3. Y. Zhou, N. Xu, Z. Luan, A. Yan, L. Wang, J. Sun, and L. Liu, Acta Opt. Sin. **29**, 2030 (2009).
4. L. Liu, Y. Zhou, Y. Zhi, J. Sun, Y. Wu, Z. Luan, A. Yan, L. Wang, E. Dai, and W. Lu, Acta Opt. Sin. **37**, 09001121 (2011).
5. B. Krause, J. Buck, C. Ryan, D. Hwang, P. Kondratko, A. Malm, A. Gleason, and S. Ashby, in *Proceedings of OSA/CLEO/QELS* (2011), paper PDPB7.
6. E. Dai, J. Sun, A. Yan, Y. Zhi, Y. Zhou, Y. Wu, and L. Liu, Acta Opt. Sin. **32**, 0528003 (2012).
7. L. Liu, Acta Opt. Sin. **32**, 0920002 (2012).
8. L. Liu, Appl. Opt. **52**, 579 (2013).
9. Z. Lu, J. Sun, Y. Zhi, Y. Zhou, F. Liu, and L. Liu, Acta Opt. Sin. **34**, 0828002 (2014).
10. Z. Zhao, J. Wu, Y. Su, N. Liang, and H. Duan, Chin. Opt. Lett. **12**, 091101 (2014).
11. Z. Luan, J. Sun, Y. Zhi, Y. Zhou, L. Wang, and L. Liu, Acta Opt. Sin. **34**, 0710003 (2014).
12. Z. Luan, J. Sun, Y. Zhou, L. Wang, M. Yang, and L. Liu, Chin. Opt. Lett. **12**, 111101 (2014).
13. Q. Xu, Z. Yu, J. Sun, Z. Lu, Z. Sun, and L. Liu, Proc. SPIE **9227**, 92270E (2014).